



PdIn intermetallic nanoparticles for the Hydrogenation of CO₂ to Methanol



Andrés García-Trenco^a, Anna Regoutz^b, Edward R. White^c, David J. Payne^b,
Milo S.P. Shaffer^{c,*}, Charlotte K. Williams^{a,*}

^a Chemistry Research Laboratory, University of Oxford, Chemistry Research Laboratory, 12 Mansfield Road, Oxford, OX1 3TA, UK

^b Department of Materials, Imperial College London, London, SW7 2AZ, UK

^c Department of Chemistry, Imperial College London, London, SW7 2AZ, UK

ARTICLE INFO

Article history:

Received 17 May 2017

Received in revised form 19 July 2017

Accepted 24 July 2017

Available online 25 July 2017

Keywords:

PdIn catalysts

PdIn intermetallics

Nanoparticles

Methanol synthesis

CO₂ hydrogenation

In₂O₃

ABSTRACT

Direct hydrogenation of CO₂ to methanol could offer significant environmental benefits, if efficient catalysts can be developed. Here, bimetallic Pd–In nanoparticles show good performance as catalysts for this reaction. Unsupported nanoparticles are synthesised by the thermal decomposition of Pd(acetate)₂ and In(acetate)₃ precursors in a high boiling point solvent (squalane), followed by reduction using dilute H₂ gas (210 °C). Adjusting the ratio of the two metallic precursors allow access to 5–10 nm nanoparticles with different phase compositions, including metallic Pd(0), In₂O₃ and intermetallic PdIn. Liquid phase methanol synthesis experiments (50 bar, 210 °C, H₂:CO₂ = 3:1) identify the intermetallic PdIn nanoparticles as the most efficient. The catalysts exhibit around 70% higher methanol rates (normalised to the overall molar metal content) compared to the conventional heterogeneous Cu/ZnO/Al₂O₃ catalyst (900 and 540 μmol mmol_{PdInorCuZnAl}^{−1} h^{−1}, respectively). In addition, the optimum Pd/In catalyst shows an improved methanol selectivity over the whole temperature range studied (190–270 °C), reaching >80% selectivity at 270 °C, compared to only 45% for the reference Cu/ZnO/Al₂O₃ catalyst. Experiments showed an improvement in stability; the methanol production rate declined by 20% after 120 h run for the optimum PdIn-based compared with 30% for the Cu/ZnO/Al₂O₃ catalyst (after 25 h). The optimum catalyst consists of ~8 nm nanoparticles comprising a surface In-enriched PdIn intermetallic phase as characterised by XRD, HR-TEM, STEM-EDX and XPS. Post-catalysis analysis of the optimum catalyst shows that the same PdIn bimetallic phase is retained with only a slight increase in the nanoparticle size.

© 2017 The Authors. Published by Elsevier B.V. This is an open access article under the CC BY license (<http://creativecommons.org/licenses/by/4.0/>).

1. Introduction

In the last decades, anthropogenic carbon dioxide (CO₂) emissions have become the focus of attention due to the implications for climate change. In this context, the hydrogenation of CO₂ to methanol, using H₂ produced from renewable energy or off peak loadings, is an attractive potential route to recycling CO₂. Methanol is an interesting fuel as it can be used directly or blended with conventional fuels, or as a generic liquid-energy carrier. It is also important in the production of chemicals such as formaldehyde, ethylene, propylene, dimethyl ether, acetic acid, and may be applied in fuel cell applications [1–3]. Indeed, methanol is one of the

top ten industrial commodity chemicals, with a global production higher than 50 million ton per year [1–3].

Methanol is industrially produced at elevated pressures (5–10 MPa) and temperatures (200–270 °C) from syn-gas (CO/CO₂/H₂) over heterogeneous catalysts based on the ternary Cu/ZnO/Al₂O₃ system [4–6]. Despite the fact that modelling studies and isotopic labelling suggested that CO₂ is the source of methanol [7,8], the need of CO in the feed is explained by the transformation of CO into CO₂ removing undesired water via the water-gas shift reaction WGS, CO + H₂O ⇌ CO₂ + H₂ [9,10]. Cu/ZnO/Al₂O₃ catalysts are active for the direct hydrogenation of pure CO₂ to methanol (CO₂ + 3H₂ ⇌ CH₃OH + H₂O), however, the catalysts show only a moderate activity, as well as low methanol selectivity and stability [3,11,12]. The limited catalytic performance is typically attributed to the catalysts also showing activity for the competitive reverse water gas shift reaction (rWGS) [13], to the inhibited activity by the by-product water [10,14], and to catalyst sintering under the reaction conditions [15]. Therefore,

* Corresponding authors.

E-mail addresses: m.shaffer@imperial.ac.uk (M.S.P. Shaffer), charlotte.williams@chem.ox.ac.uk (C.K. Williams).

new catalyst formulations have been developed and systems based on Pd/Ga₂O₃ [16–19], Au/ZnO [20], Pd/ZnO [21], Cu/CeO₂ [22], or In₂O₃ [11], all show promise. Among them, In₂O₃ nanoparticles (NPs) supported onto ZrO₂ have recently shown high activity and selectivity, as well as good stability [11]. However, these catalysts operate best at above 270 °C, indeed high temperatures are required to obtain methanol yields comparable to those from the Cu/ZnO/Al₂O₃ catalysts, but under these conditions the thermodynamic equilibrium disfavors the formation of methanol and thereby reduces the CO₂ conversion [23].

Fisher and Muhler and co-workers reported colloidal mixtures of Cu and ZnO NPs for the liquid-phase synthesis of methanol from syn-gas [24–27]. We were inspired by this approach and have reported a series of Cu/ZnO colloidal catalysts some of which show promising performance for the liquid phase hydrogenation of CO₂ to methanol [28–30]. The catalyst preparations allow production of small NPs that lead to an intimate intermixing of the Cu/ZnO components increasing the quantity of Cu/ZnO interfaces, where the active sites for the methanol synthesis are proposed to be located [31,32]. More generally, colloidal catalysts offer a broad range of possibilities to ‘tune’ or control properties such as the composition, particle size, solubility and functionality [33]. In addition, the use of a liquid reaction medium may facilitate heat removal and enable the reaction to be performed isothermally, minimising catalyst deactivation commonly attributed to a poor temperature control [5]. Recently, we extended the use of colloidal Cu/ZnO catalysts to bimetallic Pd–Ga NPs for the hydrogenation of CO₂ to methanol [34]. The resulting Pd₂Ga-based colloids showed an improved activity and stability compared to the reference Cu/ZnO/Al₂O₃ catalysts. Nevertheless, a significant rWGSr activity (CO production) was observed, at the expense of the methanol selectivity. Interestingly, the novel synthetic methodology used, consisting of the simple thermal decomposition and further reduction of organometallic precursors (Pd(II) acetate and Ga(III) stearate) is relevant to the production of other catalytic systems, as will be demonstrated here.

Bimetallic nanoparticles have recently shown great potential for catalysing reduction and oxidation reaction [35]. Supported intermetallic Pd–In compounds have shown good performances for methanol steam reforming (MSR) [36–39]; this process is simply the reverse of methanol synthesis from CO₂ (CH₃OH + H₂O ⇌ CO₂ + 3H₂), driven under different operating conditions (typically 300–450 °C and atmospheric pressure) [38,40,41]. Remarkably, the Pd/In materials are highly CO₂ selective, showing low activity for methanol decomposition (CH₃OH ⇌ CO + 2H₂) and rWGSr reactions [39,41]. The catalysts are also known to be more stable and resistant to sintering than the conventional Cu-based systems [41,42]. Despite this excellent performance in the closely related MSR process, intermetallic Pd–In catalysts have not yet been explored for the hydrogenation of CO₂ to methanol. In this work, dispersions of unsupported bimetallic Pd–In NPs are prepared and investigated for the first time in the liquid phase hydrogenation of CO₂ to methanol. The Pd–In catalysts are characterised both before and after reaction, and the catalytic performance correlated with composition and nano-scale structure.

2. Experimental section

2.1. Catalyst preparation and catalytic experiments

Both the catalyst synthesis and the catalytic studies were conducted in a 300 mL continuous flow stirred tank reactor (CSTR, Parr), mechanically stirred at 1500 r.p.m., and with vertical baffles to ensure the homogenous mixing of the gas and liquid phase. The catalysts were prepared by modifying a recently reported method

for the synthesis of Pd₂Ga NPs [34]. In a typical preparation procedure, the required amount of Pd(II) acetate (Pd(OAc)₂, Acros Organics 47.5% Pd metal basis) and In(III) acetate (In(OAc)₃, Aldrich 99.99% metal basis) were added to the stainless steel vessel containing squalane (100 mL, 3.18, mmol_{Pd+In} L⁻¹, specific quantities available in Table S1). Squalane (16 ppm water by Karl Fischer titration, Acros Organics 99%) is reported to be an excellent solvent for the liquid phase methanol synthesis [43]. The air was swept from the reactor containing squalane and the catalyst precursors by a flow of N₂ gas at 750 mL min⁻¹ for 15 min. Then, the reactor was pressurised to 0.5 MPa with N₂, and held at 210 °C (4.5 °C min⁻¹) under a N₂ flow (400 mL min⁻¹) for 1 h. Finally, the flow was switched to 200 mL min⁻¹ of 5% H₂/N₂ (vol%) for 2 h. The resulting catalysts are labelled as PdIn_x:y, where x:y is the Pd:In molar ratio used. Mixtures obtained before the 5% H₂/N₂ treatment are labelled as PdIn_x:yN₂.

To conduct the methanol synthesis experiments, the prepared Pd/In catalysts (still in the CSTR) were subjected to 5.0 MPa, 190–270 °C, and 4.7–18.9 L mmol_{Pd+In}⁻¹ h⁻¹ of a gas mixture comprising 96 vol% (75% H₂:25% CO₂) and 4 vol% Ar (internal standard for GC analysis) for 15 h.

A commercial CuO/ZnO/Al₂O₃ methanol synthesis catalyst precursor from Alfa Aesar (45776, mass composition CuO; 63.5%, ZnO; 25.1%, Al₂O₃; 10.1%, MgO; 1.3%), ground from pellet to fine powder, was tested as a reference material. The total amount of metal (Cu + Zn + Al + Mg) was kept the same as in the Pd/In catalysts (3.18 mmol_{metal} L⁻¹). Before the runs were performed, the precursor was activated by using a 5% H₂/N₂ stream at 0.45 MPa and 240 °C (2 °C min⁻¹) for 3 h, according to a standard activation procedure for Cu/ZnO/Al₂O₃ methanol synthesis catalysts in slurry reactors [44]. Finally, the catalytic experiment was performed under the same conditions described above.

The reaction products and unreacted material were analysed by an on-line gas chromatograph (Bruker 450-GC), equipped with a thermal conductivity detector (TCD), for the quantification of CO, CO₂ and Ar, and a flame ionization detector (FID), for the quantification of MeOH, and other oxygenates or hydrocarbons (if produced). Product condensation in the transfer lines from the reactor to the injection port of the GC was prevented by heating them at 180 °C. The catalytic results are given as the methanol peak rate (normalised per Pd + In or Cu + Zn + Al + Mg molar content), once the pseudo-steady state was reached, typically after ca. 7 h time-on-stream. Selectivities remained nearly constant throughout each experiment. All the experiments were conducted under differential reaction conditions, with CO₂ conversions always below 3%. Under the reaction conditions employed, the maximum CO₂ conversions calculated at the thermodynamic limit (Aspen plus v 8.8 software), considering the methanol synthesis and the side rWGSr, were 36.9, 31.8, 26.4 and 24.3% at 190, 210, 240 and 270 °C, respectively. All catalytic experiments were, therefore, performed in the kinetically-controlled regime in this study. Selectivities are given on a carbon basis, and the standard deviations determined by repeated runs was ±14% and ±2% for the methanol activity and selectivity, respectively.

Turnover frequencies (TOFs), as mol_{CH₃OH} m⁻² s⁻¹, were estimated from the average size of the Pd(0), In₂O₃ or PdIn NPs determined by TEM, and assuming a spherical shape of the NPs. For the reference Cu/ZnO/Al₂O₃ catalyst, the methanol rate is generally correlated to the initial Cu(0) surface area [6,42], and therefore, the TOF was calculated from the average Cu(0) particle size after activation determined by XRD (6.3 nm, Fig. S1). In this case, Scherrer analysis of the XRD data was used owing to agglomeration of the heterogeneous Cu/ZnO/Al₂O₃ catalyst hampering comprehensive TEM analysis.

2.2. Characterisation techniques

Thermogravimetric analysis (TGA) was performed in a Mettler Toledo TGA/DSC 1, coupled with an integrated Hiden HPR-20 QIC EGA mass spectrometer (MS), under a flow of N_2 from 100 to 700 °C, using a heating rate of 10 °C min⁻¹. Additional experiments simulated the temperature profile during the synthesis of the Pd/In catalysts, by heating from room temperature to 210 °C (4.5 °C min⁻¹), and then maintaining this temperature for 3 h under N_2 flow.

Powder X-ray diffraction (XRD) was carried out using an X'pert Pro MPD diffractometer (PANalytical B. V) operating at 40 kV and 40 mA, using nickel-filtered $Cu K\alpha$ radiation ($\lambda = 0.1542$ nm). The samples were covered by a polyimide film tape (Agar Scientific), so as to prevent contact with air during the measurements. The average crystallite size of Pd(0), PdIn, In_2O_3 and Cu(0) particles were determined by applying the Scherrer equation (shape factor of 0.9) to the most intense and not overlapped reflections at 40.2° (111), 39.3° (110), 51.3° (440) and 43.5° (111), respectively. The diffraction patterns are shown after baseline correction.

Transmission electron microscopy (TEM) samples were prepared by drop-casting a toluene solution onto a 300 mesh Au holey carbon grid with an ultrathin 3 nm carbon film (Agar Scientific). Annular dark field scanning TEM (ADF-STEM) and energy dispersive X-ray (EDX) mapping were performed with a JEOL JEM 2100F scanning transmission electron microscope operated at 200 kV, and equipped with an Oxford X-Max 80 SDD EDX detector. High-resolution TEM (HR-TEM) images were obtained with an aberration-corrected FEI Titan operated at 300 kV. For HR-TEM imaging, samples were loaded and sealed into a Gatan Environmental Holder, under a nitrogen atmosphere in a glove box, preventing any atmospheric exposure that might lead to inadvertent sample oxidation during transfer to the microscope. The average NP sizes were determined using HR-TEM and ADF-STEM by measuring approximately 200 NPs from the images of each sample. The Pd:In composition was determined by EDX performing 13–18 measurements over large, independent regions of the samples (Table S2). The method used for phase identification, as well as (*hkl*) reflections and the corresponding lattice spacings used are described in Table S2.

The surface of the samples was characterised using X-ray photoelectron spectroscopy (XPS). The spectra were recorded on a Thermo Scientific K-Alpha⁺ X-ray photoelectron spectrometer system operating at 2×10^{-9} mbar base pressure. This system incorporates a monochromated, microfocused Al $K\alpha$ X-ray source ($h\nu = 1486.6$ eV) and a 180° double focusing hemispherical analyser with a 2D detector. The X-ray source was operated with a 6 mA emission current and 12 kV anode bias and a flood gun was used to minimize sample charging. Samples were mounted using conductive carbon tape and transferred to the spectrometer using a special glove box module which ensured that samples were never exposed to air. Data were collected at 20 eV pass energy for core level (Pd 3d, In 3d, and In 4d), for In MNN Auger, and for valence band spectra using an X-ray spot size of 400 μm^2 . All data were analysed using the Advantage software package. For the calculation of the inelastic electron mean free path (IMFP) following the Tanuma, Powell and Penn (TPP-2M) method, the QUASES software package was used [45].

With the aim of preventing any air exposure, Pd/In pre- and post-catalysis samples analysed by XRD, XPS, and TEM were prepared using air-sensitive techniques. As such, the samples were withdrawn from the reactor to a Schlenk tube, under a N_2 atmosphere, via a cannula and a high flow rate of N_2 (400 mL min⁻¹), washed several times with dry toluene (distilled from sodium

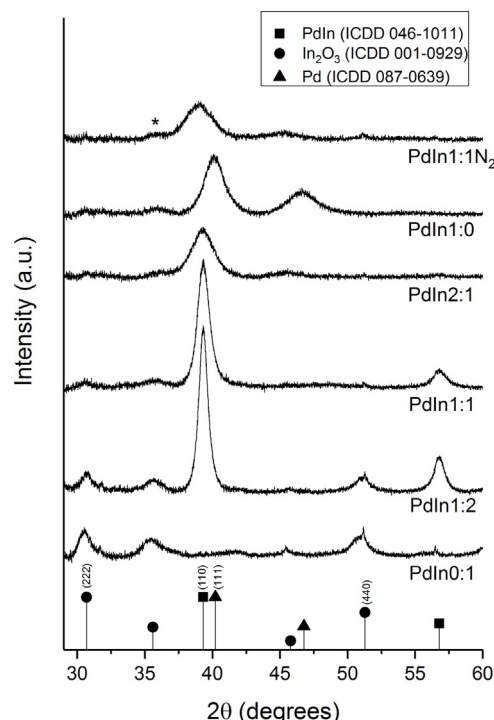


Fig. 1. XRD patterns for Pd/In samples at different stages in the preparation, and with different Pd:In composition. *Diffraction from the polyimide film tape used to prevent the air-exposure of the samples.

and degassed by performing at least three free-pump-thaw cycles, $O_2 < 5$ ppm), and subsequently dried under vacuum (10^{-2} Pa).

3. Results and discussion

3.1. Formation of the Pd/In catalysts

In the first synthetic step, a mixture of the $Pd(OAc)_2$ and $In(OAc)_3$ (Pd:In molar ratio of 1:1) in squalane was treated at 210 °C and 0.5 MPa N_2 , for 1 h. The TGA-MS data indicate that, after 1 h at this temperature, the thermal decomposition of $Pd(OAc)_2$ is complete, whereas $In(OAc)_3$ is only partially decomposed (Fig. S2). The degradation of the precursors mostly leads to the formation of acetic acid (boiling point 180 °C at 0.5 MPa), acetone (boiling point 113 °C at 0.5 MPa) and CO_2 (Fig. S3–S4), which are expected to be released from the reaction medium under the N_2 flow (400 mL min⁻¹). XRD of the resulting black suspension, sample PdIn1:1N₂, revealed only the presence of Pd(0) crystallites, with a cubic F structure and an average diameter of 3.8 nm, whereas no diffraction peaks for In-containing phases are observed (Fig. 1, Table 1). Interestingly, the PdIn1:1N₂ peaks are shifted ($\sim 0.9^\circ$) to lower 2θ angles compared to the ICDD 087-0639 reference pattern, which can be attributed to an expansion in the Pd-Pd interatomic distance for Pd(0) crystallites of such a small size [46]. TEM analysis also confirmed the presence of Pd(0) NPs with an average size of 5.4 ± 0.5 (1.2) nm (Fig. S5), although in this case, a few In_2O_3 NPs (< 5 nm) were also identified (Fig. S6). The low concentration of In_2O_3 NPs along with their expected small crystallite size is likely responsible for the absence of any observable In_2O_3 diffraction peaks in the corresponding XRD. The formation of separate metallic Pd(0) and In_2O_3 phases from the thermal decomposition of $Pd(OAc)_2$ and $In(OAc)_3$, under a N_2 atmosphere, is consistent with previous publications [47,48].

Next, the mixture was subjected to a dilute H_2 flow, at 210 °C for 2 h, and the XRD pattern of the resulting suspension (sample PdIn1:1) showed only diffraction peaks attributed to the forma-

Table 1
HR-TEM and XRD characterisation results of the Pd:In samples.

Sample	HR-TEM		XRD	Primary crystalline Phase	Secondary crystalline Phase
	Pd:In ratio ^a (standard deviation)	Average particle size (nm) ^{b,c} (standard deviation)			
PdIn1:1N ₂	1.35 ± 0.07 (0.2)	5.4 ± 0.5 (1.2)	3.8	Pd(0)	In ₂ O ₃
PdIn1:0	–	6.0 ± 0.4 (1.8)	5.1	Pd(0)	–
PdIn2:1	1.90 ± 0.2 (0.6)	7.8 ± 0.6 (2.4)	4.2	PdIn	–
PdIn1:1	0.99 ± 0.02 (0.06)	10.1 ± 0.8 (2.8)	8.2	PdIn	In ₂ O ₃
PdIn1:2	0.47 ± 0.02 (0.10)	11.5 ± 0.9 (3.2)	10.5	PdIn	In ₂ O ₃
PdIn0:1	–	2.1 ± 0.1 (0.9)	5.4	In ₂ O ₃	–

^a Pd:In molar ratio determined from EDX analysis. The standard error of the mean was defined as standard deviation/sqrt (n° measures), and does not account for systematic errors in the k-factors used in standardless quantification which can be ~10%.

^b The standard error of the mean was defined as standard deviation/sqrt (n° measures).

^c Size values for the primary crystalline phase.

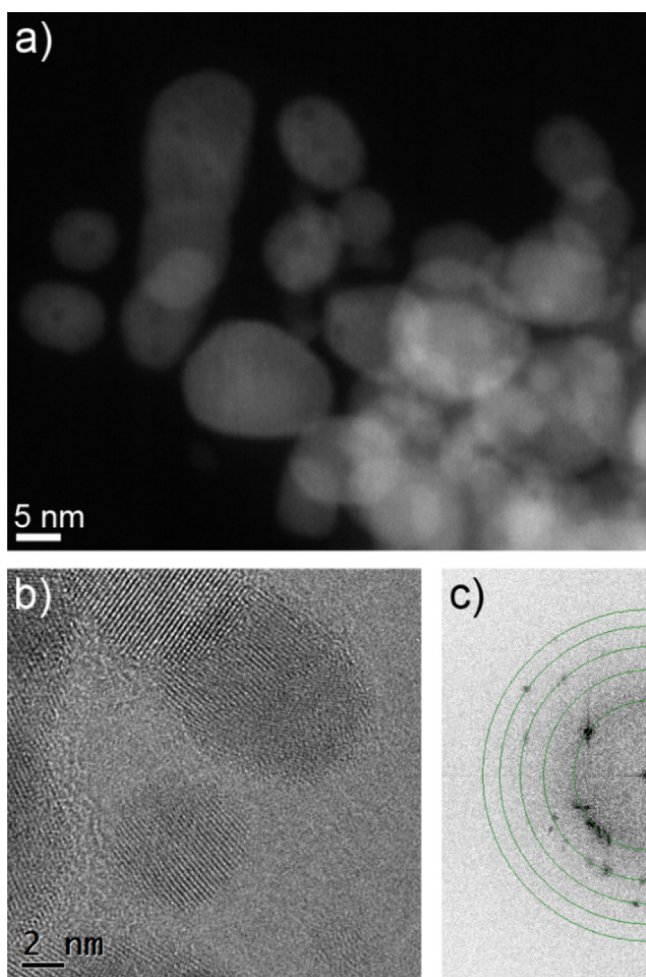


Fig. 2. a) Representative ADF-STEM, and b) HR-TEM images showing PdIn NPs in PdIn1:1 sample. c) FFT of b. The rings indicate the reciprocal lattice distances corresponding to the 110, 200, 211, 220, 310 PdIn *hkl* reflections.

tion of a PdIn crystalline phase, with a cubic CsCl structure (Fig. 1). The increased sharpness of the reflexions indicates an increase in the average crystallite size, which was determined to be from 3.8 to 8.2 nm. Assuming a 33% radius expansion upon In incorporation (based on the metals relative densities), it is clear that some ripening must also take place. HR-TEM (Fig. 2) identified spherical NPs with an average size of 10.1 ± 0.8 (2.8) nm (Table 1). Lattice spacing analysis of the NPs (both in Fig. 2), and the Pd:In composition determined by EDX (Table 1) were also consistent with the formation of the PdIn intermetallic alloy. Interestingly, a con-

trol experiment using the same synthesis protocol but including only In(OAc)₃ precursor (sample PdIn0:1), did not show any In(0)-containing phases; rather, the In(III) species were only reduced in presence of Pd(0) under the relevant conditions. Analogous observations have been reported for Pd/Ga systems [49], where it is proposed that Pd(0), either through hydrogen dissociation or by forming active hydrides [50,51], mediates the reduction of Ga(III) species which subsequently diffuse into the Pd(0) core to form Pd-Ga alloy.

3.2. Influence of the Pd/In composition

A series of samples were prepared varying the Pd:In composition. As determined by EDX, the average Pd:In molar ratios for the samples, after the two preparation steps, were consistent with the expected values assuming the conversion of the Pd and In precursors into the In- and Pd-containing phases. During the first step of the synthesis under N₂, the In(OAc)₃ precursor decomposes at a slow rate (see TGA, Fig. S2) and is only completely decomposed after the second preparation step (H₂/N₂ treatment). In agreement with this hypothesis, the PdIn1:1N₂ sample, submitted only to the first step, contained a higher than expected Pd:In ratio (1.35) presumably due to the removal of some unreacted In(OAc)₃ during work-up. As observed by XRD (Fig. 1), the use of the Pd(OAc)₂ alone (PdIn1:0) produced a metallic Pd(0) phase with an average crystallite size of 5.1 nm (Table 1). The pure In(OAc)₃ yielded a product (PdIn0:1) consisting of In₂O₃ crystallites of 5.6 nm. The presence of small crystalline In₂O₃ NPs in this PdIn0:1 sample was also identified by HR-TEM (Fig. S7). XRD patterns for the samples containing both Pd and In mainly showed diffraction peaks attributed to the formation of the PdIn intermetallic phase, revealing larger crystallites with increasing In content, in accordance with TEM. As expected, the sample with excess In (PdIn1:2), shows also small diffraction peaks corresponding to In₂O₃, in addition to the PdIn intermetallic phase. Strikingly, the sample with an excess of Pd (PdIn2:1) exhibited only the PdIn phase, as also observed by HR-TEM (Fig. S8). Interestingly, in this case, many of observed NPs consisted of several PdIn crystalline domains (Fig. S8), which explains the larger discrepancy between the particle sizes ascertained by XRD and HR-TEM, for this PdIn2:1 sample, 4.2 and 7.8 ± 0.6 (2.4) nm, respectively. Previous work identified the formation of the CsCl-structured PdIn intermetallic, in preference to other possible phases across a range of stoichiometries [52]; in that case, excess Pd was proposed to form a core within the PdIn shell structures under Pd rich conditions. However, in the current system there is no evidence of a significant Pd(0) component in XRD, HR-TEM or XPS characterisation. Rather, XPS analysis for the PdIn 2:1 sample is more consistent with the formation of an In-deficient form of the PdIn intermetallic (*vide infra*).

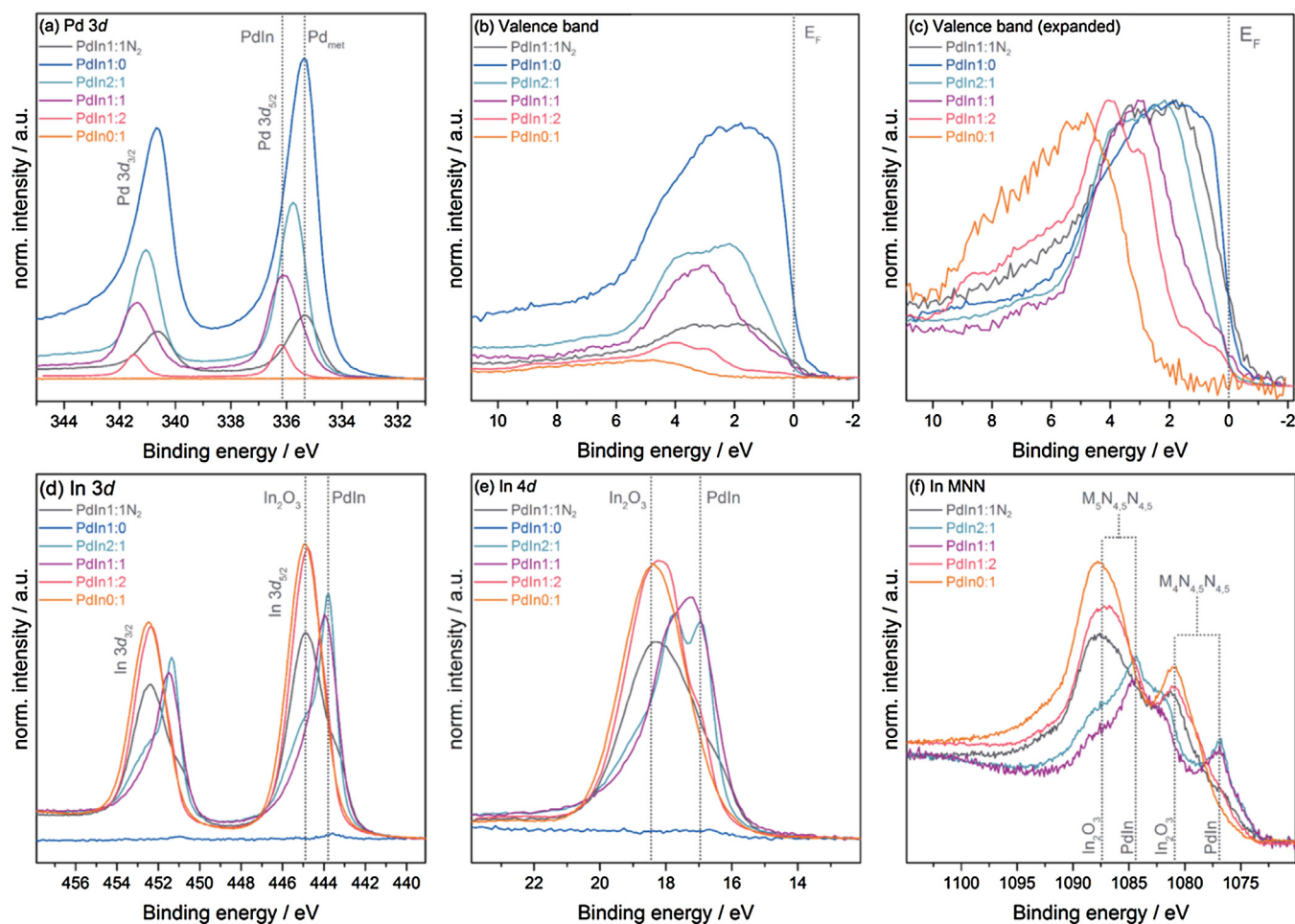


Fig. 3. XPS spectra for Pd/In samples at different preparation steps and with different Pd/In ratios, including (a) Pd 3d core level, (b) valence band spectrum, (c) expanded valence band spectrum, (d) In 3d core level, (e) In 4d core level, and (f) In M_{4.5}N_{4.5}N_{4.5} Auger lines. All spectra (except (c)) were normalised using the total combined area of In 3d_{5/2} and Pd 3d_{5/2}, (c) shows an expanded view of the valence band normalised to maximum intensity.

3.3. XPS characterisation

The nature of the Pd and In species after submitting the precursors to the thermal treatment, sample PdIn1:1N₂, was studied by XPS analysis. The Pd 3d core level is dominated by the characteristic asymmetric line shape and binding energy position (BE = 335.3 eV) of Pd(0) (Fig. 3(a)), in agreement with reports in the literature [53–55]. In addition, the valence band (Fig. 3(b) and (c)) shows a high density of states at the Fermi energy E_F, typical for Pd(0), which stems from Pd 4d states [51,55]. The In core levels (Fig. 3(d) and (e)) are dominated by higher BE components at 444.3 eV (In 3d_{5/2}) and 18.3 eV (In 4d_{5/2}), which indicate the presence of In(III) in In₂O₃ [53,55,56]. Second, lower BE components are assigned to In alloy environments (443.3 eV in In 3d_{5/2} and 16.4 eV in In 4d_{5/2}). The In M_{4.5}N_{4.5}N_{4.5} Auger lines further confirm the observation of a mixed In(0)/In(III) oxidation state (Fig. 3(f)). The overall line shapes and peak positions of Pd and In 3d for the sample PdIn1:1N₂ point towards a mixed system dominated by metallic Pd(0) and In₂O₃, which is in accordance with previous XRD and HR-TEM characterisation. However, in this case, a small contribution from PdIn intermetallic alloy phase was observed. Peak fit analysis of the In and Pd 3d_{5/2} core levels indicates a clear surface enrichment of In, with an overall Pd:In molar ratio of 27:73 compared to 57:43 found from EDX analysis, mainly suggesting that the In₂O₃ species are on the surface of the Pd(0) NPs (Fig. 4, Tables 1 and S3).

Having established the spectra of the Pd(0) and In₂O₃ phases, the full range of samples reduced in H₂ (PdIn1:0, PdIn2:1, PdIn1:1,

PdIn1:2, PdIn0:1) was also investigated using XPS (Fig. 3). A clear transition from Pd(0) to the Pd-In intermetallic phase can be observed in the Pd 3d core level. For the PdIn1:0 sample (not containing In) the core line shows the characteristic asymmetric line shape of Pd(0), which is directly related to a large local density of states at the Fermi energy E_F caused by Pd 4d states. The peak maximum is at a BE of 335.3 eV. Upon addition of In, the asymmetry is lost, as the Pd 4d band shifts away from E_F, and a continuous shift to higher BE is observed. In addition, a narrowing of the Pd 3d peak is observed upon alloying consistent with previous reports [55]. The PdIn1:1 and PdIn1:2 samples have final 3d_{5/2} BEs of 336.1 and 336.2 eV, respectively, which are consistent with the formation of the PdIn intermetallic phase observed with XRD and HR-TEM. For the PdIn2:1 sample, XPS shows one symmetric component to the Pd core line at an intermediate BE (335.9 eV) between Pd(0) and the PdIn intermetallic phase. This intermediate BE position implies an In-deficiency of the PdIn intermetallic alloy, and is in agreement with gradual changes in Pd BE positions previously reported for the transition from Pd to In-rich intermetallic alloy phases [54,56]. Although an excess of Pd was used to form the PdIn intermetallic phase, no indication of metallic Pd(0) can be found, in agreement with the results from XRD and TEM.

The In 3d and 4d core levels show a clear grouping between the different catalyst samples. The In 3d and 4d spectra of PdIn2:1 and PdIn1:1 are dominated by the intermetallic phase at BEs of 443.8 eV and 17.0 eV, respectively, with only a small contribution from In₂O₃. In contrast, the spectra of the PdIn1:2 and PdIn0:1 sam-

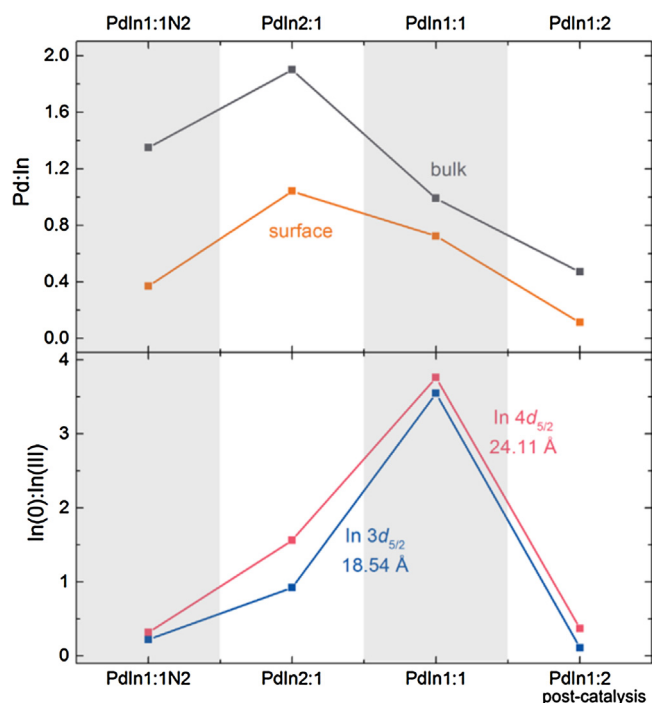


Fig. 4. Overall surface Pd:In and In(0):In(III) atomic ratio for the Pd/In samples compared to the bulk atomic ratio determined by EDX. The surface ratios were calculated from peak fits to the Pd 3d_{5/2}, In 3d_{5/2}, and In 4d_{5/2} core levels from XPS measurements.

ples mainly consist of signal from In₂O₃ at BEs of 444.8 eV (In 3d_{5/2}) and 18.4 eV (In 4d_{5/2}). Both the peak positions for In 3d_{5/2} in the alloy and the oxide agree very well with values reported in the literature for Pd–In systems [41,53–56]. The In M_{4,5}N_{4,5}N_{4,5} Auger lines further confirm these findings, exhibiting typical line shapes of either In(0) or In₂O₃. Reference spectra for the In M_{4,5}N_{4,5}N_{4,5} Auger lines are scarce, but the observed energy positions are in agreement with two reports by Lin et al. and Nichols et al. [57,58] Auger parameters α after Gaarenstrom and Winograd [59] from the In 3d_{5/2} core level and the M₅N_{4,5}N_{4,5} Auger level were determined to be 846.0 ± 0.2 eV for the intermetallic phase and 844.0 ± 0.2 eV for the oxide phase.

Valence band (VB) spectra (Fig. 3(b) and (c)) clearly reflect the change in surface chemistry of the catalyst samples following the transition from metallic Pd in PdIn1:0 to In₂O₃ in PdIn0:1. The pure Pd sample has a large density of states at the Fermi energy E_F, which is lost with increasing In content. Already in the PdIn2:1 sample, there is a clear shift of the VB maximum away from E_F. The overall shape of the valence band of the PdIn1:1 sample is often described as Cu-like as the states above 1.5 eV appear very similar to those of Cu [54,56,60]. Three distinct regions can be identified within the valence band of the Pd–In intermetallic alloy and by comparison with theoretical calculations for the density of states (DOS) [60,61] their orbital character can be identified. Above 5 eV, low intensity states stemming from In 5s and Pd 4d are observed. The large contribution to the DOS between 5 and 2 eV is dominated by Pd 4d with some In 5p (and a very small contribution from Pd s states). Finally, the intensity from 2 eV up to the Fermi energy E_F is again caused by a mixture of Pd 4d and In 5p states. The non-zero intensity at E_F leads to a metal-like behaviour of the In–Pd alloy. This change from Pd-like to Cu-like valence states has been reported previously upon transition from Pd-rich to In-rich intermetallic phases [54–56]. Finally, an excess of In in the PdIn1:2 sample leads to a strong contribution from In₂O₃ states to the VB above 4 eV, which can be compared to the pure In sample (PdIn0:1) [62,63].

From peak fits to the Pd and In 3d_{5/2} core lines, overall atomic ratios of Pd:In could be determined (Table S1). In all samples, a surface enrichment of In is observed compared to the ratios determined by EDX analysis (Table 1). In order to study the In speciation of this enrichment, relative ratios of the In(0) and In(III) components for the In 3d_{5/2} and 4d_{5/2} core lines were determined. Due to the difference in the kinetic energy E_K of the photoelectrons, with ΔE_K in the order of 400 eV, a variation in the In(0):In(III) ratio was found. The surface sensitivity of the two signals is different, with In 3d being more surface sensitive than In 4d. Using the Tanuma, Powell and Penn (TPP-2M) method, the inelastic electron mean free path (IMFP) was calculated, which is a good measure for the depth sensitivity of certain core levels [45]. As a close approximation the IMFP values were correlated for In₂O₃ at average binding energies of the In 3d_{5/2} and 4d_{5/2} core levels of 445 eV and 18 eV, respectively. Calculations based on these values result in a 30% higher IMFP for In 4d_{5/2}, with the exact values being 18.54 Å for In 3d_{5/2} and 24.11 Å for In 4d_{5/2}. As the intensity of the In₂O₃ component is comparatively larger in the In 3d than in the 4d core level, it can be concluded that the surface of the PdIn intermetallic NPs is enriched with In₂O₃. Analogous Ga₂O₃ enrichment was found for Pd₂Ga NPs prepared by a similar method [34]. The PdIn1:1 sample is the only mixed Pd/In sample dominated by the intermetallic alloy contributions for both core levels.

3.4. Catalytic experiments

3.4.1. Influence of the Pd/In composition

The different Pd/In-based catalysts were tested in the liquid phase hydrogenation of CO₂ to methanol at 210 °C and 5.0 MPa. Typically, after 7 h of stabilisation, the catalyst showed a very low loss in activity, and nearly constant selectivity with TOS. The only co-product detected was CO, derived from the competitive rWGS. As summarised in Fig. 5, the PdIn1:0 catalyst, consisting of Pd(0) NPs, is barely active for the methanol synthesis, whereas the catalyst based on In₂O₃ NPs (PdIn0:1) shows a modest activity. Nevertheless, the combination of Pd and In leads to a dramatic enhancement in the methanol rate, reaching a maximum for the Pd:In molar ratio of 1:1 (PdIn1:1). Significantly, the optimum methanol rate is about 67% higher than that for the benchmark Cu/ZnO/Al₂O₃ (900 and 540 μmol mmol_{PdIn}orCuZnAl^{−1} h^{−1}, respectively), when normalising for the total molar metal content (Pd + In or Cu + Zn + Al + Mg). Since this most active catalyst consists of PdIn NPs (see section 3.1), it is clear that this bimetallic phase is particularly suited for the hydrogenation of CO₂ to methanol. In order to normalise the methanol synthesis activity in terms of surface area, the TOF, as mol_{MeOH} m^{−2} s^{−1}, were estimated (Fig. 5) considering the NP size of the main phase (Table 1). The TOFs of the Pd/In samples clearly differed according to the Pd:In composition, leading to a maximum for the catalysts PdIn1:1 and PdIn1:2. The similar TOF (within the error) suggest that once there is enough In to form the PdIn alloy, any further addition of In, which leads to the formation of In₂O₃ NPs, has no substantial impact on the methanol synthesis activity. In fact, In₂O₃ NPs (sample PdIn0:1) exhibited a negligible TOF under the reaction conditions studied. The optimum TOFs are quite similar to that obtained for the reference Cu/ZnO/Al₂O₃ catalyst, normalised to the Cu(0) surface area [6,42].

Currently, there are no reports investigating the nature of the methanol synthesis active sites upon formation of the PdIn intermetallic phase. Nevertheless, simultaneous changes in the electronic and structural properties of the materials can be assumed. The higher activity of the Pd–In intermetallic phases respect to the corresponding isolated pure metallic or oxide phases (Pd(0) or In₂O₃) has also been reported for the methanol steam reforming process [38,41]. Some studies, using both unsupported

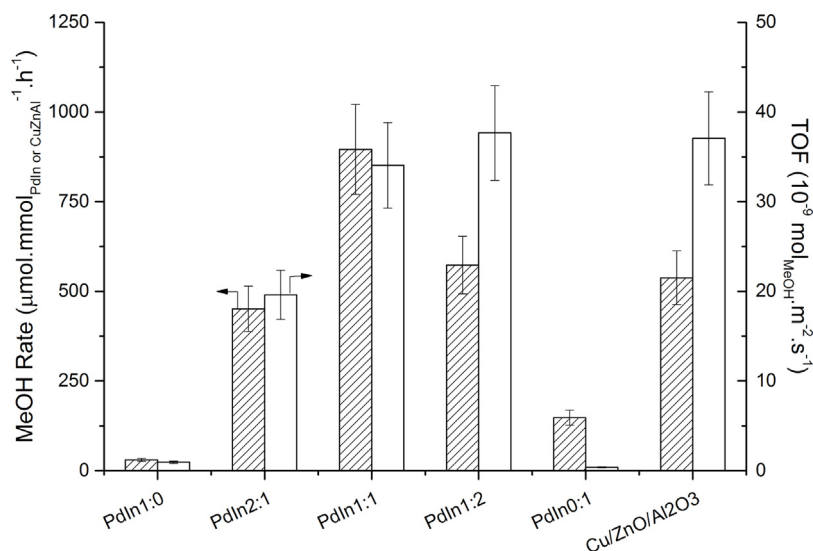


Fig. 5. Methanol synthesis rate and TOF of the Pd/In-based catalysts varying the Pd:In molar ratio. The reference Cu/ZnO/Al₂O₃ catalyst is included as reference. Reaction conditions: 210 °C, 5.0 MPa, GHSV = 18.9 L.mmol_{PdInorCuZnAl}⁻¹ h⁻¹ and CO₂/H₂ = 3/1.

PdIn intermetallic catalysts, as well as PdIn supported on In₂O₃, have attributed the enhancement in methanol steam reforming activity to a bimetal-oxide (PdIn-In₂O₃) synergy [37,56,64]. Interestingly, a synergistic mechanism was also reported for bimetallic PdGa NPs supported on Ga₂O₃ in the hydrogenation of CO₂ to methanol, where the role of the bimetallic PdGa NPs is to provide atomic hydrogen via spillover to the reaction intermediates adsorbed on Ga₂O₃ [17]. It is also worth noting that oxygen vacancies in In₂O₃, whose concentration can be modulated by co-feeding CO or using supports like zirconia, have been recently reported to be active sites for the methanol synthesis from CO₂ [11]. As observed by XPS analysis (section 3.3), the surface of all the Pd/In-containing catalysts was enriched in In₂O₃ species. Although the current study does not rigorously exclude a possible promotion of the methanol synthesis activity by the In₂O₃ species, there was no relationship between the surface concentration of In₂O₃ species and the intrinsic activity.

Catalysts with PdIn1:1, PdIn1:2 and PdIn0:1 exhibited an excellent methanol selectivity, with values always above 90% (Fig. S9). No CO was detected for the catalyst based on In₂O₃ NPs (PdIn0:1), either, in agreement with a recent publication [11]. However, the very low activity of this PdIn0:1 catalyst means that any CO production may be close to the GC detection limit. Interestingly, the sample PdIn2:1, with an In-deficient PdIn intermetallic alloy, revealed a dramatic drop in methanol selectivity (51% MeOH) in favour of CO selectivity (49%). Some authors have attributed the CO production to the rWGS activity of unalloyed Pd(0) in catalysts for the methanol synthesis or methanol steam reforming [38,65]. However, in this case, the catalyst based on Pd(0) NPs (PdIn1:0) was not active for the rWGS (no CO production) under the reaction conditions employed here, which is in agreement with some other studies [34,66]. The origin of the higher CO production observed for PdIn2:1 is still not clear, however, it can be tentatively attributed to the different electronic or structural properties of the In-deficient PdIn intermetallic phase, as revealed the characterisation results (section 3.2). Some authors have proposed that changes in selectivity upon PdIn intermetallic are due to the diluting effect of the In which ensures that no adjacent Pd atoms are present on the surface, leading to the formation of new active sites [52]; further studies are expected to shed light on this aspect.

3.4.2. Influence of the operation conditions and stability

The performance of the optimum PdIn1:1 catalyst for the CO₂ hydrogenation to methanol reaction was also compared to the benchmark Cu/ZnO/Al₂O₃ catalyst, across the temperature range 190–270 °C (Fig. 6a). The methanol rate for the PdIn1:1 catalyst reaches a maximum at 240 °C. The subsequent drop in rate at higher reaction temperatures can be mostly explained by the ripening of the PdIn NPs. In fact, XRD analysis of the catalyst NPs after the reaction at 270 °C indicated an average PdIn crystallite diameter of 16.6 nm (Fig. S10), around 105% higher than the original catalyst. Apart from this run at 270 °C, the PdIn1:1 catalyst showed methanol rates 50–100% higher than those for the reference Cu/ZnO/Al₂O₃ material at a given reaction temperature. Remarkably, the increase in rate is 110% at 190 °C, which highlights the potential of the PdIn intermetallic phase to carry out the methanol synthesis process from CO₂ at lower temperatures. Both PdIn1:1 and Cu/ZnO/Al₂O₃ catalysts experienced a drop in methanol selectivity with increasing reaction temperature, as expected due to the more favourable rWGS (*vide infra*). Only the runs at 270 °C produced any alkanes, in the form of a small amount of CH₄ and short chain hydrocarbons (C₂–C₄), with a total selectivity lower than 5%. Interestingly, the methanol selectivity for the PdIn1:1 catalyst is significantly higher than that for the reference Cu/ZnO/Al₂O₃ catalyst across the entire temperature range studied. In fact, the methanol selectivity for the Pd/In catalysts only dropped from 96 (190 °C) to 83% (270 °C), whereas the methanol selectivity for the Cu/ZnO/Al₂O₃ system decreased from 94 (190 °C) to 44% (270 °C).

From Arrhenius plots (Fig. S11), the apparent activation energies for the methanol synthesis and rWGS were calculated from the MeOH and CO production rates. Apparent activation energies of 41 and 117 kJ mol⁻¹ were obtained for methanol and CO formation on Cu/ZnO/Al₂O₃, respectively, agreeing well with reported values [19,67]. In comparison, the PdIn1:1 catalyst exhibited a similar apparent activation energy for the methanol synthesis (35 kJ mol⁻¹), but a substantially lower value for the rWGS (76 kJ mol⁻¹). The lower activation energy for the rWGS would indicate a lower methanol selectivity for the PdIn1:1 catalyst compared to Cu/ZnO/Al₂O₃ unless the occurrence of the corresponding active sites is much lower. Interestingly, the lower activation energy for the CO formation indicates that the methanol selectivity is relatively less sensitive to changes in temperature than for the conventional catalyst. In contrast to the proposed similarities in

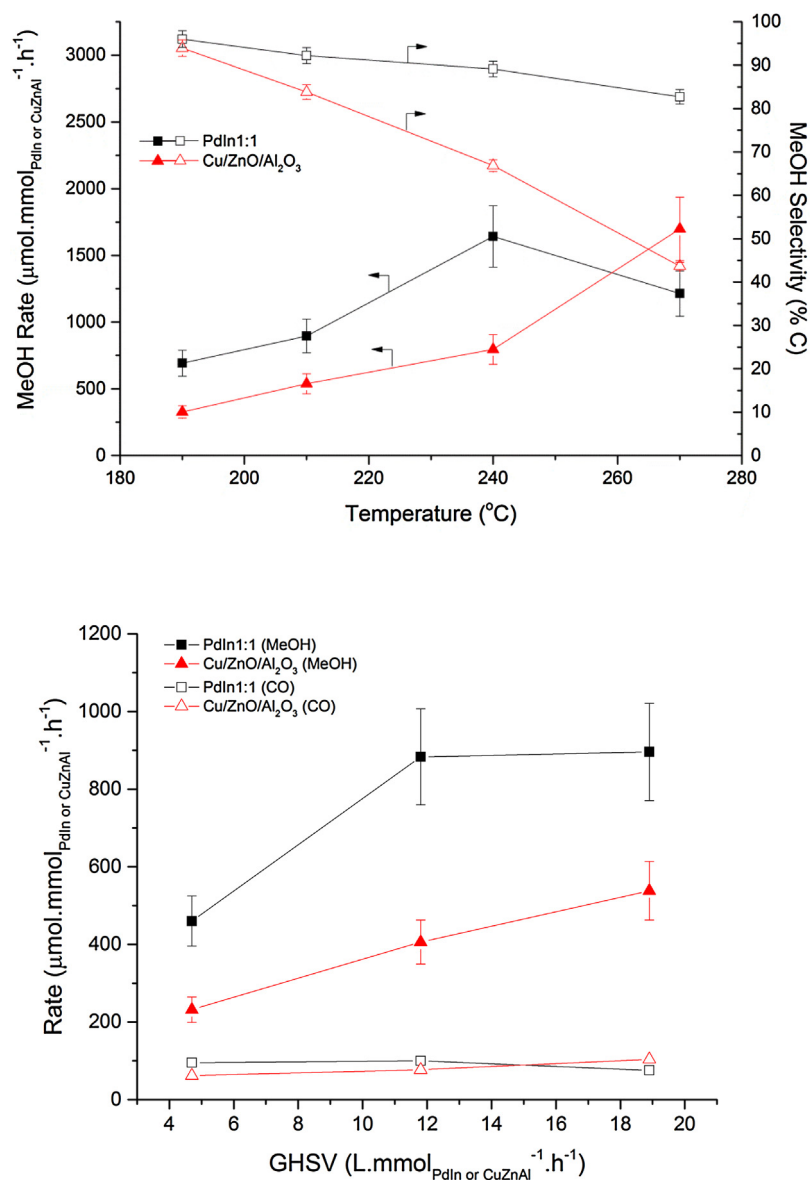


Fig. 6. a) Methanol synthesis rate and selectivity of the Pd/In and Cu/ZnO/Al₂O₃ catalyst at 190–270 °C. Reaction conditions: 5.0 MPa, GHSV = 18.9 L mmol_{PdIn or CuZnAl}⁻¹ h⁻¹ and CO₂/H₂ = 3/1. b) Influence of the space velocity on the MeOH and CO rates. Reaction conditions: 5.0 MPa and CO₂/H₂ = 3/1.

the reaction pathway to form methanol for both catalytic systems, the differing apparent activation energies for the rWGS suggest mechanistic differences. Analogous differences in the apparent activation energies for the rWGS were found for bimetallic Pd-Ga catalysts compared to the conventional Cu/ZnO/Al₂O₃ when used in the hydrogenation of CO₂ to methanol [19].

In the case of Cu/ZnO/Al₂O₃ catalysts used in the hydrogenation of CO₂ to methanol, decreased space velocity is known to reduce the methanol rate and selectivity [14,19,20]. This phenomenon is typically attributed to a product inhibition effect (mainly water) [14,19,20]. To explore this aspect, the optimum PdIn1:1 and the reference Cu/ZnO/Al₂O₃ catalysts were studied at 210 °C and 5.0 MPa varying the inlet flow (Fig. 6b). Upon decreasing the flow rate, and thus, increasing the concentration of the reaction products in the medium, the methanol rate drastically decreases for both catalytic systems. Nevertheless, the methanol rate of the PdIn1:1 catalyst only appears to be affected when using space velocities lower than 12 L mmol_{PdIn or CuZnAl}⁻¹ h⁻¹. On the other hand, the CO rate is clearly more stable to changes in the space velocity for both catalysts. As a consequence, the methanol selectivity decreases, as expected,

from 92 (18.9 L mmol_{metal}⁻¹ h⁻¹) to 83% (4.7 L mmol_{metal}⁻¹ h⁻¹) for the PdIn1:1 catalyst, and from 85 (18.9 L mmol_{metal}⁻¹ h⁻¹) to 79% (4.7 L mmol_{metal}⁻¹ h⁻¹) for the Cu/ZnO/Al₂O₃ catalyst. The results suggest that the active sites for methanol synthesis are product-inhibited, for both catalytic systems.

The short term stabilities of the PdIn1:1 and the reference Cu/ZnO/Al₂O₃ catalyst were assessed by testing the catalyst for 25 h time-on-stream at 210 °C and 5.0 MPa (Fig. S12). The Cu/ZnO/Al₂O₃ catalyst deactivated by ~30% over this period, a well-known effect which is typically attributed to the sintering of the Cu and ZnO phases [11,68]. In contrast, the methanol rate of the PdIn1:1 sample dropped by only ~15%, indicating a substantial improvement in stability. The metal ratio of the PdIn1:1 post-catalysis material determined by EDX analysis was 0.90 ± 0.01(0.05), compared to 0.99 ± 0.02(0.06) for the fresh catalyst; thus, within error, there is no change in average Pd:In composition during the catalytic run, although low levels of leaching cannot be completely excluded. XRD characterisation of the PdIn1:1 post-catalysis material revealed only the presence of the PdIn intermetallic crystallite phase (Fig. S13), in accordance with the diffraction patterns

obtained from the HR-TEM images (Fig. S14). The results indicate that the crystalline structure of the sample is preserved during the reaction. Nonetheless, both techniques showed a slight increase in the crystallite/NP size from 8.2 to 11.6 nm by XRD, and from 10.1 ± 0.8 to 11.1 ± 0.8 nm by TEM. Therefore, the loss in the methanol synthesis rate can be mostly attributed to the reduction in the effective surface area related to ripening of the NPs. Finally, with the aim of studying the long term stability of the optimum PdIn1:1 catalyst, the reaction was studied for 120 h on stream. The methanol rate decreased by ~20% for the first 30 h and then remained at a constant value (Fig. S15). These results confirmed an improvement in stability compared to Cu/ZnO/Al₂O₃ catalyst even after 120 h. At the end of the extended reaction, the PdIn remained the only phase identified by XRD, although the crystallites were ripened to an average of 14.4 nm (Fig. S13); most of this coarsening occurred during the first 25 h time on stream. In order to reduce the ripening of the nanoparticles in the reaction liquid medium, ligands may be introduced to provide steric stabilisation in the future.

4. Conclusions

Dispersions of unsupported Pd-In bimetallic NPs have been prepared, simply and effectively, using a two-step procedure. In the first step, Pd(OAc)₂ and In(OAc)₃ (1:1 molar ratio) were thermally treated at 210 °C under N₂ flow, leading to the formation of Pd(0) NPs of ca. 4 nm. In the second step, the resulting mixture was reduced under a diluted H₂ flow at 210 °C, yielding Pd-In intermetallic alloy NPs of ca. 8 nm, attributed to the Pd-mediated reduction of the In(III) species and their subsequent diffusion into the core of the Pd(0) NPs. XRD and HR-TEM consistently identified the PdIn intermetallic phase. Exploiting the surface sensitivity of XPS analysis, In₂O₃ species were identified on the surface of the resulting intermetallic NPs. Various control NP catalysts were prepared using different Pd/In ratios of the precursors, including the pure Pd(0) and In₂O₃ systems.

Catalytic experiments using dispersions of the unsupported Pd/In-based NPs with different compositions were tested in the liquid phase hydrogenation of CO₂ to methanol (H₂:CO₂ of 3:1 and 50 bar). Pure Pd(0) or In₂O₃ NPs were hardly active, whereas the catalyst containing PdIn intermetallic NPs showed a dramatic increase in the methanol synthesis activity. Interestingly, among Pd/In catalysts, the use of excess Pd to form the PdIn phase (Pd:In molar ratio of 2:1) reduced methanol synthesis activity and selectivity (50%), whereas the catalyst consisting of PdIn intermetallic NPs (Pd:In = 1:1) showed the maximum methanol rate, which is ~70% higher than that for the conventional Cu/ZnO/Al₂O₃ catalyst, based on overall metal molar content (Pd + In or Cu + Zn + Al), and >90% methanol selectivity. This optimum catalyst was studied versus the reference Cu/ZnO/Al₂O₃ catalyst under different reaction conditions. Runs at 190–270 °C showed a substantial improvement in the methanol synthesis activity and selectivity (low CO production) compared to the conventional catalyst. In fact, the methanol selectivity was higher than 80% at the highest studied temperature (270 °C), whereas the conventional catalyst gave values as low as 45%. Further, the optimum Pd/In catalyst exhibited somewhat higher stability than the Cu/ZnO/Al₂O₃ catalyst for 120 h time-on-stream. The PdIn intermetallic phase was retained in the post-catalysis sample, although with a slight increase in the NP size. Finally, a space velocity study indicated that the reaction is product inhibited for both catalytic systems (Pd/In and Cu/ZnO/Al₂O₃).

Considering the continued interest in using CO₂ as a feedstock, and the strong performance (activity, selectivity and stability) of the unsupported PdIn intermetallic NPs, there is potential to develop further catalysts. Further studies of catalytic active sites and pos-

sible mechanisms are expected to guide improvements to the catalytic systems for methanol synthesis.

Acknowledgements

The EPSRC is acknowledged for funding (EP/H046380, EP/K035274/1, EP/M013839/1, EP/M028291/1). D.J.P. acknowledges support from the Royal Society (UF100105) and from the EPSRC (EP/K004913/1 and EP/J021199/1).

Appendix A. Supplementary data

Supplementary data associated with this article can be found, in the online version, at <http://dx.doi.org/10.1016/j.apcatb.2017.07.069>.

References

- [1] G.A. Olah, A. Goepfert, G.S. Prakash, *Beyond Oil and Gas: The Methanol Economy*, John Wiley & Sons, 2011.
- [2] M. Bertau, H. Offermanns, L. Plass, F. Schmidt, H.-J. Wernicke, *Methanol: The Basic Chemical and Energy Feedstock of the Future*, Springer, 2014.
- [3] S.G. Jadhav, P.D. Vaidya, B.M. Bhanage, J.B. Joshi, *Chem. Eng. Res. Des.* 92 (2014) 2557–2567.
- [4] J.B. Hansen, P.E. Højlund Nielsen, *Methanol Synthesis*, in: *Handbook of Heterogeneous Catalysis*, Wiley-VCH, 2008, pp. 2920–2949, 13:13.13.
- [5] S. Lee, A. Sardesai, *Top. Catal.* 32 (2005) 197–207.
- [6] C. Baltes, S. Vukojević, F. Schüth, *J. Catal.* 258 (2008) 334–344.
- [7] G. Chinchin, P. Denny, D. Parker, M. Spencer, D. Whan, *Appl. Catal.* 30 (1987) 333–338.
- [8] G. Dutta, A.A. Sokol, C.R.A. Catlow, T.W. Keal, P. Sherwood, *ChemPhysChem* 13 (2012) 3453–3456.
- [9] Y. Zhang, Q. Sun, J. Deng, D. Wu, S. Chen, *Appl. Catal. A* 158 (1997) 105–120.
- [10] F. Studt, M. Behrens, E.L. Kunkes, N. Thomas, S. Zander, A. Tarasov, J. Schumann, E. Frei, J.B. Varley, F. Abild-Pedersen, *ChemCatChem* 7 (2015) 1105–1111.
- [11] O. Martin, A.J. Martín, C. Mondelli, S. Mitchell, T.F. Segawa, R. Hauert, C. Drouilly, D. Curulla-Ferré, J. Pérez-Ramírez, *Angew. Chem. Int. Ed.* 55 (2016) 6261–6265.
- [12] M. Kurtz, H. Wilmer, T. Genger, O. Hinrichsen, M. Muhler, *Catal. Lett.* 86 (2003) 77–80.
- [13] J. Nakamura, Y. Choi, T. Fujitani, *Top. Catal.* 22 (2003) 277–285.
- [14] M. Sahibzada, I. Metcalfe, D. Chadwick, *J. Catal.* 174 (1998) 111–118.
- [15] M.B. Fichtl, D. Schlereth, N. Jacobsen, I. Kasatkin, J. Schumann, M. Behrens, R. Schlögl, O. Hinrichsen, *Appl. Catal. A* 502 (2015) 262–270.
- [16] E.M. Fiordaliso, I. Sharafutdinov, H.W.P. Carvalho, J.-D. Grunwaldt, T.W. Hansen, I. Chorkendorff, J.B. Wagner, C.D. Damsgaard, *ACS Catal.* 5 (2015) 5827–5836.
- [17] S.E. Collins, J.J. Delgado, C. Mira, J.J. Calvino, S. Bernal, D.L. Chiavassa, M.A. Baltanás, A.L. Bonivardi, *J. Catal.* 292 (2012) 90–98.
- [18] X. Zhou, J. Qu, F. Xu, J. Hu, J.S. Foord, Z. Zeng, X. Hong, S.C.E. Tsang, *Chem. Commun.* 49 (2013) 1747–1749.
- [19] L. Li, B. Zhang, E. Kunkes, K. Föttinger, M. Armbrüster, D.S. Su, W. Wei, R. Schlögl, M. Behrens, *ChemCatChem* 4 (2012) 1764–1775.
- [20] Y. Hartadi, D. Widmann, R.J. Behm, *J. Catal.* 333 (2016) 238–250.
- [21] H. Bahruji, M. Bowker, G. Hutchings, N. Dimitratos, P. Wells, E. Gibson, W. Jones, C. Brookes, D. Morgan, G. Lalev, *J. Catal.* 343 (2016) 133–146.
- [22] J. Graciani, K. Mudiyanse, F. Xu, A.E. Baber, J. Evans, S.D. Senanayake, D.J. Stacchiola, P. Liu, J. Hrbek, J.F. Sanz, *Science* 345 (2014) 546–550.
- [23] Q. Sun, Y.-L. Zhang, H.-Y. Chen, J.-F. Deng, D. Wu, S.-Y. Chen, *J. Catal.* 167 (1997) 92–105.
- [24] S. Schimpf, A. Rittermeier, X. Zhang, Z.-A. Li, M. Spasova, M.W.E. van den Berg, M. Farle, Y. Wang, R.A. Fischer, M. Muhler, *ChemCatChem* 2 (2010) 214–222.
- [25] A. Rittermeier, S. Miao, M.K. Schröter, X. Zhang, M.W. van den Berg, S. Kundu, Y. Wang, S. Schimpf, E. Löffler, R.A. Fischer, *Phys. Chem. Chem. Phys.* 11 (2009) 8358–8366.
- [26] M.K. Schröter, L. Khodeir, M.W. van den Berg, T. Hikov, M. Cokoja, S. Miao, W. Grünert, M. Muhler, R.A. Fischer, *Chem. Commun.* (2006) 2498–2500.
- [27] M.A. Sliem, S. Turner, D. Heeskens, S.B. Kalidindi, G. Van Tendeloo, M. Muhler, R.A. Fischer, *Phys. Chem. Chem. Phys.* 14 (2012) 8170–8178.
- [28] N.J. Brown, A. García-Trenco, J. Weiner, E.R. White, M. Allinson, Y. Chen, P.P. Wells, E.K. Gibson, K. Hellgardt, M.S.P. Shaffer, C.K. Williams, *ACS Catal.* 5 (2015) 2895–2902.
- [29] N.J. Brown, J. Weiner, K. Hellgardt, M.S.P. Shaffer, C.K. Williams, *Chem. Commun.* 49 (2013) 11074–11076.
- [30] A. García-Trenco, E.R. White, M.S.P. Shaffer, C.K. Williams, *Catal. Sci. Technol.* 6 (2016) 4389–4397.
- [31] A. Le Valant, C. Comminges, C. Tisseraud, C. Canaff, L. Pinard, Y. Pouilloux, *J. Catal.* 324 (2015) 41–49.
- [32] E. Poels, D. Brands, *Appl. Catal. A* 191 (2000) 83–96.

- [33] D. Astruc, F. Lu, J.R. Aranzas, *Angew. Chem. Int. Ed.* 44 (2005) 7852–7872.
- [34] A. García-Trenco, E.R. White, A. Regoutz, D.J. Payne, M.S.P. Shaffer, C.K. Williams, *ACS Catal.* 7 (2017) 1186–1196.
- [35] M. Sankar, N. Dimitratos, P.J. Miedziak, P.P. Wells, C.J. Kiely, G.J. Hutchings, *Chem. Soc. Rev.* 41 (2012) 8099–8139.
- [36] N. Iwasa, T. Mayanagi, N. Ogawa, K. Sakata, N. Takezawa, *Catal. Lett.* 54 (1998) 119–123.
- [37] H. Lorenz, S. Turner, O.I. Lebedev, G. Van Tendeloo, B. Klötzer, C. Rameshan, K. Pfalter, S. Penner, *Appl. Catal. A* 374 (2010) 180–188.
- [38] Y. Men, G. Kolb, R. Zapf, M. O'Connell, A. Ziogas, *Appl. Catal. A* 380 (2010) 15–20.
- [39] C. Rameshan, W. Stadlmayr, S. Penner, H. Lorenz, L. Mayr, M. Hävecker, R. Blume, T. Rocha, D. Teschner, A. Knop-Gericke, *J. Catal.* 290 (2012) 126–137.
- [40] H. Lorenz, C. Rameshan, T. Biele, N. Memmel, W. Stadlmayr, L. Mayr, Q. Zhao, S. Soisuwan, B. Klötzer, S. Penner, *ChemCatChem* 5 (2013) 1273–1285.
- [41] M. Neumann, D. Teschner, A. Knop-Gericke, W. Reschtilowski, M. Armbrüster, *J. Catal.* 340 (2016) 49–59.
- [42] S. Sá, H. Silva, L. Brandão, J.M. Sousa, A. Mendes, *Appl. Catal. B* 99 (2010) 43–57.
- [43] G.P. van der Laan, A.A. Beenackers, B. Ding, J.C. Strikwerda, *Catal. Today* 48 (1999) 93–100.
- [44] A. Sawant, M.K. Ko, V. Parameswaran, S. Lee, C.J. Kulik, *Fuel Sci. Technol. Int.* 5 (1987) 77–88.
- [45] S. Tanuma, C.J. Powell, D.R. Penn, *Surf. Interface Anal.* 21 (1994) 165–176.
- [46] T. Teranishi, M. Miyake, *Chem. Mater.* 10 (1998) 594–600.
- [47] Y. Sawada, T. Shigaraki, S. Seki, M. Ogawa, T. Senda, T. Nishide, J.-i. Matsushita, *J. Mass Spec. Soc. Jpn.* 46 (1998) 292–295.
- [48] T. Tano, K. Esumi, K. Meguro, *J. Colloid Interface Sci.* 133 (1989) 530–533.
- [49] M. Armbrüster, G. Wowsnick, M. Friedrich, M. Heggen, R. Cardoso-Gil, *J. Am. Chem. Soc.* 133 (2011) 9112–9118.
- [50] A. Borodziński, A. Janko, *React. Kinet. Catal. Lett.* 7 (1977) 163–169.
- [51] A. Haghofer, K. Föttinger, F. Girgsdies, D. Teschner, A. Knop-Gericke, R. Schlögl, G. Rupprechter, *J. Catal.* 286 (2012) 13–21.
- [52] Z. Wu, E.C. Wegener, H.-T. Tseng, J.R. Gallagher, J.W. Harris, R.E. Diaz, Y. Ren, F.H. Ribeiro, J.T. Miller, *Catal. Sci. Technol.* 6 (2016) 6965–6976.
- [53] S. Furukawa, M. Endo, T. Komatsu, *ACS Catal.* 4 (2014) 3533–3542.
- [54] G.M. McGuirk, J. Ledieu, É. Gaudry, M.C. De Weerd, V. Fournée, *J. Chem. Phys.* 141 (2014).
- [55] T. Skála, K. Veltruská, M. Moroseac, I. Matolínová, G. Korotchenkov, V. Matolín, *Appl. Surf. Sci.* 205 (2002) 196–205.
- [56] C. Rameshan, H. Lorenz, L. Mayr, S. Penner, D. Zemlyanov, R. Arrigo, M. Hävecker, R. Blume, A. Knop-Gericke, R. Schlögl, B. Klötzer, *J. Catal.* 295 (2012) 186–194.
- [57] A.W.C. Lin, N.R. Armstrong, T. Kuwana, *Anal. Chem.* 49 (1977) 1228–1235.
- [58] G.D. Nichols, D.A. Zatko, *Inorg. Nucl. Chem. Lett.* 15 (1979) 401–404.
- [59] S.W. Gaarenstroom, N. Winograd, *J. Chem. Phys.* 67 (1977) 3500–3506.
- [60] E. Gaudry, G.M. McGuirk, J. Ledieu, V. Fournée, *J. Chem. Phys.* 141 (2014) 141–149.
- [61] M. Wencka, M. Hahne, A. Kocjan, S. Vrtnik, P. Kozelj, D. Korze, Z. Jaglicic, M. Soric, P. Popcevic, J. Ivkov, A. Smontara, P. Gille, S. Jurga, P. Tomes, S. Paschen, A. Ormeci, M. Armbrüster, Y. Grin, J. Dolinsek, *Intermetallics* 55 (2014) 56–65.
- [62] L.F.J. Piper, A. DeMasi, S.W. Cho, K.E. Smith, F. Fuchs, F. Bechstedt, C. Körber, A. Klein, D.J. Payne, R.G. Egdell, *Appl. Phys. Lett.* 94 (2009) 022105.
- [63] A. Regoutz, R.G. Egdell, D.J. Morgan, R.G. Palgrave, H. Téllez, S.J. Skinner, D.J. Payne, G.W. Watson, D.O. Scanlon, *Appl. Surf. Sci.* 349 (2015) 970–982.
- [64] H. Lorenz, C. Rameshan, T. Biele, N. Memmel, W. Stadlmayr, L. Mayr, Q. Zhao, S. Soisuwan, B. Klötzer, S. Penner, *ChemCatChem* 5 (2013) 1273–1285.
- [65] A. Ota, E.L. Kunkes, I. Kasatkin, E. Groppo, D. Ferri, B. Poceiro, R.M.N. Yerga, M. Behrens, *J. Catal.* 293 (2012) 27–38.
- [66] T. Fujitani, M. Saito, Y. Kanai, T. Watanabe, J. Nakamura, T. Uchijima, *Appl. Catal. A* 125 (1995) L199–L202.
- [67] A. Karelavic, P. Ruiz, *Catal. Sci. Technol.* 5 (2015) 869–881.
- [68] M.V. Twigg, M.S. Spencer, *Top. Catal.* 22 (2003) 191–203.